OCEANOGRAPHY

Understanding uncertainties in contemporary and future extreme wave events for broad-scale impact and adaptation planning

Joao Morim[1]*, Thomas Wahl[1], Sean Vitousek[2], Sara Santamaria-Aguilar[1], Ian Young[3], Mark Hemer[4]

Understanding uncertainties in extreme wind-wave events is essential for offshore/coastal risk and adaptation estimates. Despite this, uncertainties in contemporary extreme wave events have not been assessed, and projections are still limited. Here, we quantify, at global scale, the uncertainties in contemporary extreme wave estimates across an ensemble of widely used global wave reanalyses/hindcasts supported by observations. We find that contemporary uncertainties in 50-year return period wave heights (H_s^{50}) reach (on average) ~2.5 m in regions adjacent to coastlines and are primarily driven by atmospheric forcing. Furthermore, we show that uncertainties in contemporary H_s^{50} estimates dominate projected 21st-century changes in H_s^{50} across ~80% of global ocean and coastlines. When translated into broad-scale coastal risk analysis, these uncertainties are comparable to those from storm surges and projected sea level rise. Thus, uncertainties in contemporary extreme wave events need to be combined with those of projections to fully assess potential impacts.

INTRODUCTION

Extreme waves are a key driver of coastal change (*1*) and loss of natural coastal wetlands (*2*) and a major contributor to coastal flooding over multiple time scales (*3*, *4*), with wave run-up often representing up to ~50% of extreme total water levels along many coastlines (*3*, *5*). These events can also disrupt shipping (*6*) and are critical to establish design limits for offshore and coastal infrastructure (e.g., natural gas and oil drilling platforms, aquaculture farms, renewable energy projects, and coastal defenses) (*7*, *8*), which are forecasted to expand by up to ~50% within less than a decade (*9*, *10*). Thus, estimating and understanding uncertainties in extreme wave events for the present-day climate is critical to support global offshore and coastal developments (*10*), assess hazards and adaptation measures (*11*), and substantiate projections under future climate scenarios (*12*).

At broad spatial scales, multidecadal wave reanalysis and hindcast model products are needed for impact assessments as wave buoy records are sparsely distributed globally and have limited length, and satellite altimetry observations suffer from relatively low temporal resolution (*13*). The contribution of extreme waves to structural design loads, erosion, and flooding (via wave setup and/or run-up) is usually determined as a function of deep-water significant wave height (H_s) (*14*–*20*). Now, multiple contemporary global wave reanalysis and hindcast products, generated using different calibration data, numerical spectral wave models, and/or atmospheric (reanalysis) forcing, are being used to generate such estimates (*16*–*21*). Comparative analyses show that offshore/coastal hazard modeling estimates can change significantly depending on datasets and models adopted (*22*), which can affect policy and adaptation measures (*22*). Some former analyses, comparing specific historical years and/or specific hindcast data, suggest that extreme wave heights could also vary considerably depending on the global wave product (*23*–*25*). Nevertheless, a comprehensive global-scale uncertainty analysis of contemporary extreme H_s estimates across multiple widely used wave reanalysis/hindcast products is still missing, as previously acknowledged (*22*, *26*).

In addition, increasing evidence suggests that extreme waves are likely to considerably change across many global ocean areas and coastlines due to climate change (*27*–*29*), and such changes need to be accounted for when determining offshore and coastal impacts (*30*). For example, in the Southern Hemisphere, low-probability extreme wave events obtained using annual maxima (AMAX) H_s have been projected to increase by up to ~15% by the end of the century (*31*–*34*). However, existing projections of extreme H_s rely on single-method wave ensembles (*27*, *28*, *31*, *33*, *34*) and thus neglect any uncertainties between different statistical and/or dynamical wave simulations (*26*), which are known to account for up to ~50% of the total projection uncertainty (*26*). These projections have also been substantiated on the basis of different global wave reanalysis and hindcast model datasets (*35*). Thus, there is a need for an all-encompassing analysis of projected changes in extreme H_s events.

Understanding uncertainties in extreme wave events for the present-day climate and comparing them to potential future changes and associated uncertainties due to global climate warming are thereby critical to support planning and adaptation strategies (*22*, *36*). Here, we quantify present-day uncertainties in extreme H_s estimates using a novel ensemble of state-of-the-art global wave model products (*37*) and compare such estimates against those obtained from 64 wave buoys around the world. Furthermore, we compare the present-day uncertainties in extreme H_s estimates to projected future changes in extreme H_s and associated uncertainties obtained from the most comprehensive ensemble of global wave projections developed to date.

[1]Univeristy of Central Florida (UCF), Orlando, FL, USA. [2]Pacific Coastal and Marine Science Center, U.S. Geological Survey (USGS), Santa Cruz, CA, USA. [3]Department of Infrastructure Engineering, University of Melbourne, Parkville, Victoria, Australia. [4]Commonwealth Scientific and Industrial Research Organisation (CSIRO) Oceans and Atmosphere, Hobart, Tasmania, Australia.
*Corresponding author. Email: jmorimnascimento@ucf.edu

RESULTS

Extreme value analysis

To characterize extreme wave events, we use the AMAX approach and apply the generalized extreme value (GEV) and Gumbel (GUM) extreme value distributions, which are widely used to estimate the n-year return period H_s (henceforward H_s^n) required for offshore and coastal engineering designs (*31*–*34*). Other extreme value analysis (EVA) methods exist (e.g., peaks over threshold, r-largest, and conditional average exceedance rate) (*38*–*40*) but require hourly or sub-daily time series H_s data, which are not archived (and/or accessible) across the full global wave product ensembles (Materials and Methods; tables S1 to S3) due to computational and storage constraints. We estimate present-day H_s^n values and their confidence intervals by fitting these two extreme value distributions to the time series of AMAX H_s (GEV-AMAX and GUM-AMAX for GEV and GUM, respectively) from 12 global wave model products that span the analysis period of 35 years (1980 to 2014) (Materials and Methods). Two global wave products are wind-wave reanalyses derived using fully coupled atmosphere-wave models that assimilate satellite wave data (from 1991 onward) to adjust model predicted wave spectra. The other products are global wave hindcasts generated, at different research institutes, by directly forcing global spectral wave models with surface winds from different atmospheric reanalyses (table S1). Through this analysis, we use GUM-MAX (as reference) because it provides an overall, more suitable model for the AMAX H_s databases from both observations and model products over most of the global ocean (Materials and Methods), consistent with previous work (*33*). However, we still consider GEV-AMAX to assess uncertainties associated with the extreme value model used, as later discussed.

Comparison with observations

Model estimates of H_s^n (from GUM-AMAX) are compared with the estimates derived from 64 moored wave-buoy stations with suitable locations, record lengths, and completeness (Materials and Methods; fig. S1). In this analysis, we limit estimates to 50-year return period events (or H_s^{50}) to avoid large uncertainties associated with extrapolation to return periods far beyond the length of the wave observational records and global wave datasets used (tables S1 and S2). The comparison of return levels from observations and products shows that the spread in present-day H_s^n estimates (from different global wave model products) can be considerable and is highly variable depending on ocean regions and locations, as shown for six representative (extra-tropical and tropical) sites near major coastal cities (Fig. 1). Furthermore, spread values in present-day H_s^n product estimates become particularly larger for those events with relatively lower probability and higher-risk potential, such as H_s^{20} and longer. For instance, estimates for H_s^{50} differ by nearly 5 m off Boston, Port Canaveral, and Yokohama and 3 m off Hawaii, San Francisco, and Sydney. We also find similar spread at other representative sites (fig. S2).

When the central estimates from the global wave products are compared to the 95% confidence intervals of the GUM-AMAX estimates from the observations, we find a significant percentage of sites where 6 or more models lie within observational limits for the 50-year events (~45%) and a small percentage of sites where 10 or more models fall within the observational intervals (~7%) (Fig. 2). Furthermore, we find that no individual global wave model product leads to the lowest or highest errors compared to the observations at all sites or even within specific regions (figs. S3 and S4). Such results, along with the sparsity of global wave buoy records, preclude any weighting of individual ensemble model products based on their relative skill (Materials and Methods). Although there is a general tendency of global wave products to underestimate H_s^{50} (figs. S5 and S6), consistent with spectral wave models underestimating storm peak H_s (*23*, *24*, *41*), absolute errors relative to wave observations change significantly depending on product and location. However, some products result in smaller mean absolute errors across all locations and fall within the 95% confidence intervals of the observational records across many more locations (Fig. 2). For instance, all Climate Forecast System Reanalysis (CFSR)–based global wave products show much smaller mean absolute errors (~10%) and also lie within the observational limits far more often (~60%) compared to ECMWF-ERAI (23 and 18%), IORAS-MERRA2 (19 and 30%), and GOW1-NCEPNCAR (18 and 37%), respectively. The overlap between confidence bounds of GUM-AMAX estimates from model products and observational records was also assessed. However, at many locations, the confidence bounds estimated from both datasets are relatively large and therefore do not provide a faithful measure of how well model products represent observations.

Clustering analysis

We show that extreme H_s^{50} estimates from different global wave products (fig. S6) are clustered by atmospheric reanalysis forcing (Fig. 3). Our cluster analysis (see Materials and Methods) defines three key groups (Fig. 3A) with products using the same reanalysis forcing falling within the same cluster regardless of global wind-wave modeling method used (e.g., source-term wave parameterization, numerical resolution, and/or spectral frequency). Hence, global wave products generated using the same atmospheric reanalysis forcing lead to estimates of similar magnitude and spatial pattern (fig. S7), highlighting the strong influence of surface winds on extreme ocean wave estimates (*41*, *42*). For example, all CFSR-based wave model products lead to higher estimates, almost everywhere, compared to ERAI-driven products (see Fig. 3B). The sample space available within each cluster (see Fig. 3) precludes from quantifying within-cluster similarities and separates the influence of different global wind-wave modeling methods on extreme wave estimates. However, we still show that, even within each cluster or subcluster based on the same reanalysis forcing (e.g., CFSR or ERAI cluster), differences in contemporary H_s^{50} estimates due to wave modeling methodology (e.g., numerical scheme, resolution, spectral frequency, and/or source-term wave parameterizations) can reach up to ~3 m across widespread ocean regions (Fig. 3C).

Uncertainty analysis

We calculate the weighted ensemble mean (by forcing) of contemporary H_s^{50} (Materials and Methods) across all the global wave model products (Fig. 4A) and quantify its associated uncertainty using the ensemble interquartile range (IQR) (Fig. 4B). Our results show that IQR values exceed 1 m (and 2 m) for 50 and 79% (32 and 13%) of global ocean and coastlines, respectively (Table 1). Spatially, IQR values can extend from less than ~1 m

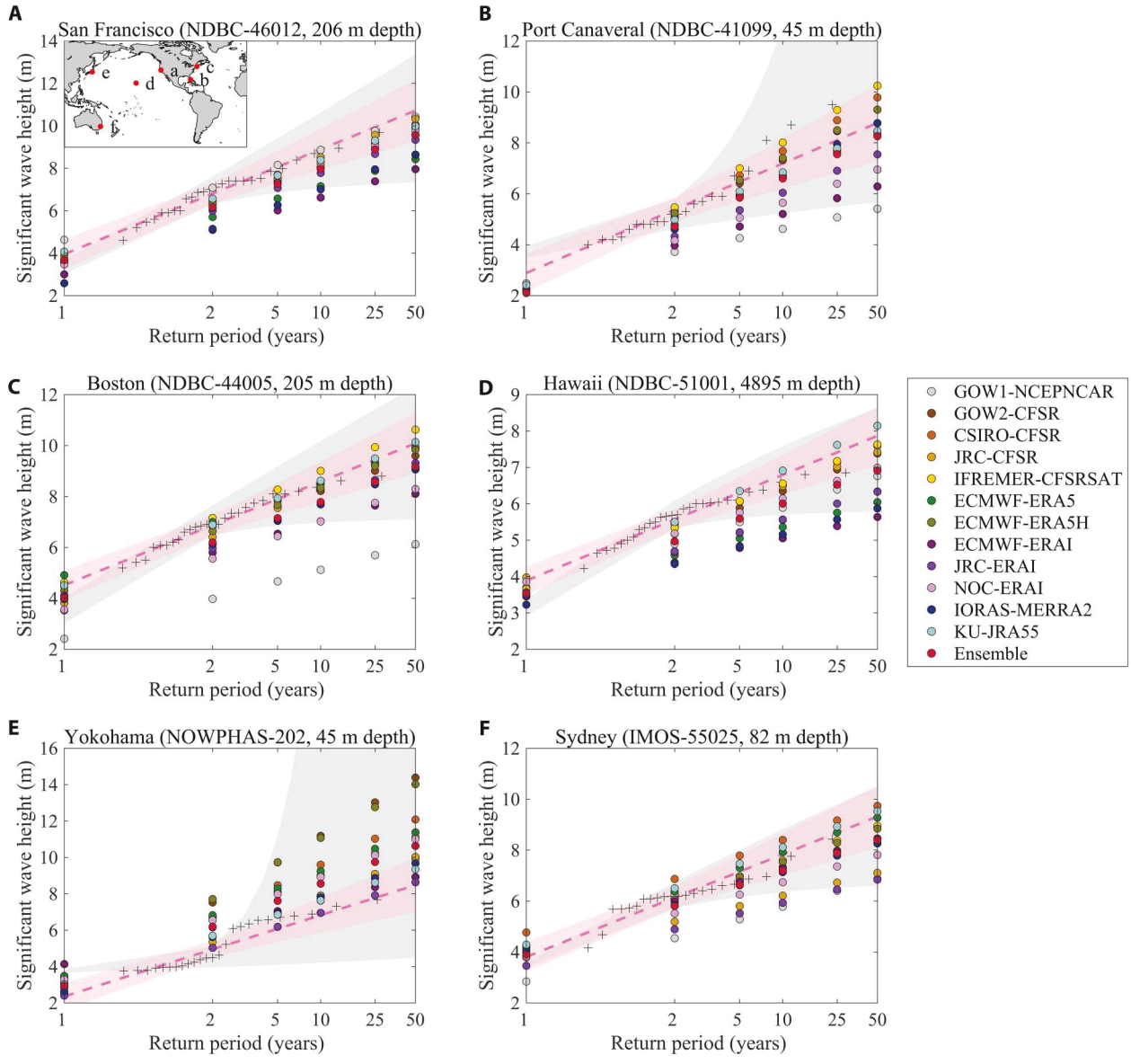

Fig. 1. Return period significant wave height (H_s^n) estimates for representative wave buoy sites off major coastal cities. (**A** to **F**) The plotting positions ("+") were obtained from the observed AMAX for each site and are hence directly comparable to the GUM-AMAX fit from the different global wave products (see circles). Shaded pink (gray) bands represent the 95% confidence limits of GUM-AMAX (GEV-AMAX) method applied to the wave observations, and the dashed line is the GUM-AMAX's central estimate. The ID code for each wave buoy station is provided within each subpanel (table S2).

within tropical areas up to ~3 m across widespread extratropical cyclone (ETC) areas and 5 m across tropical cyclone (TC)–dominated areas (Fig. 4B). The maximum difference between ensemble estimates ranges from ~3 up to ~7 m across most nontropical areas (fig. S8). Attributing the potential underlying causes for these uncertainties across the globe is beyond the analysis. However, we believe that they are largely associated with the representation of ETC and TC systems within the reanalysis datasets, given that atmospheric forcing is the major source of uncertainty among contemporary extreme H_s estimates (Fig. 3). Although ETC and TC intensities are generally underrepresented within most atmospheric reanalysis datasets relative to observational datasets, particularly TC events (*43*, *44*), specific atmospheric reanalyses can capture and resolve certain features of ETC and TC systems, such as cyclone storm tracks and/or frequency (e.g., owing to improved model resolution, data assimilation, and/or bias-correction methods) (*43*–*47*). Hence, some reanalysis-forced global wave products are more capable of resolving specific features of ETC- and/or TC-generated wave events than others (fig. S9), leading to a considerable spread among extreme wave estimates across such regions (Fig. 4B).

To date, much research has been conducted to assess uncertainties associated with EVA models used to parameterize extreme events. For example, 100-year storm surge estimates can vary by more than 0.5 m (*48*) and 100-year H_s estimates by up to ~0.5 to 1 m depending on location (*38*). Comparison of present-day H_s^{50} uncertainty due to global wave product differences with those

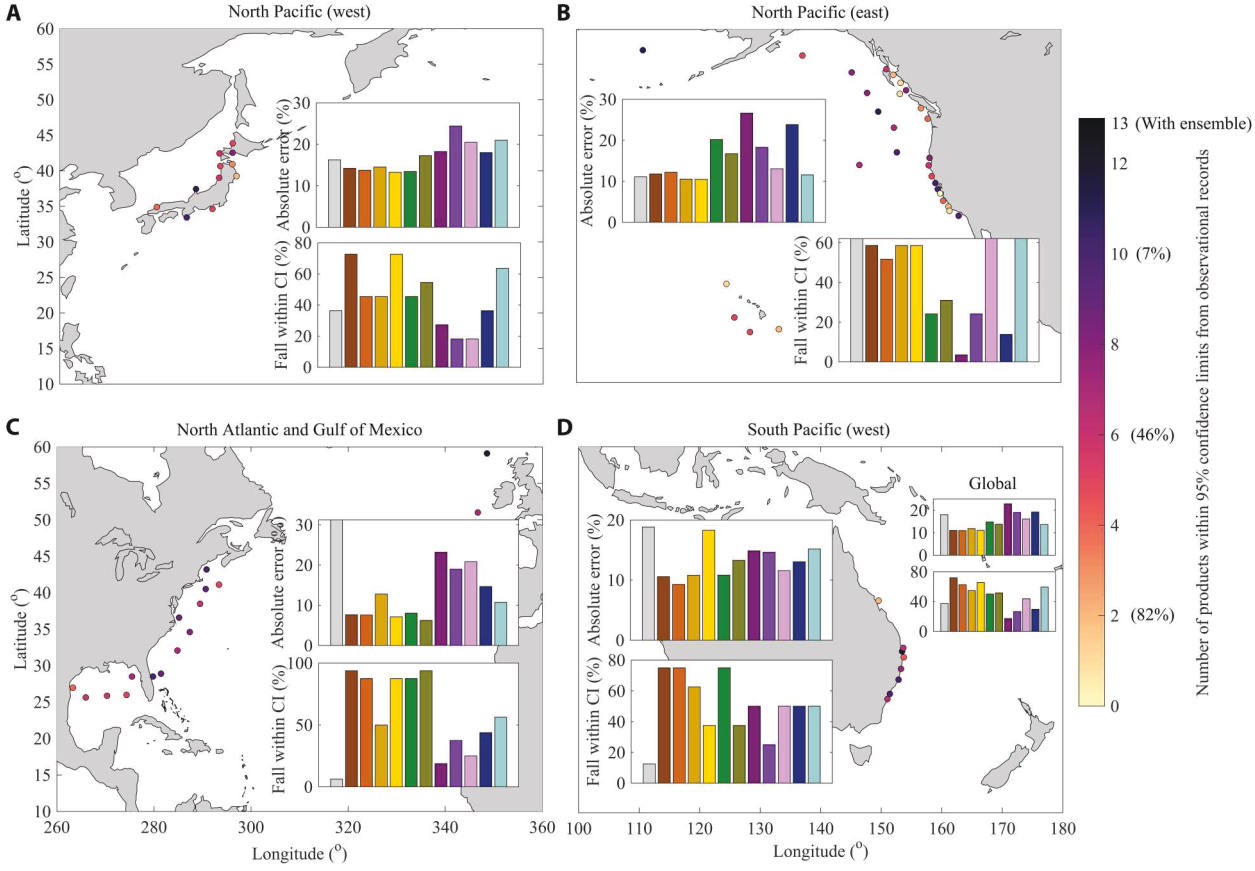

Fig. 2. Number of global wave product estimates falling within the 95% confidence limits of the observations for H_s^{50} at all wave buoy sites. (**A**) North Pacific (east), (**B**) North Pacific (west), (**C**) North Atlantic and Gulf of Mexico, and (**D**) South Pacific (west). The column chart colors (within each subplot) are consistent with the legend of Fig. 1. The percentage of sites with more than 2, 6, and 10 model estimates falling within the observational confidence intervals (CI) is also provided within brackets along the color bar scale. For each respective basin, the mean absolute error across all locations and all products is shown along with the percentage of sites that each product falls within the observational bounds.

Table 1. Uncertainty comparison across existing marine-built infrastructure sites, global ocean area and coastline length. See Materials and Methods for calculation of uncertainties.

Percentage of	Constructed offshore and coastal infrastructure			Global coastline length	Global ocean area
	Gas and oil (267)	Wind farms (26)	Ports (1045)		
Present-day uncertainty (IQR) > 1 m (2 m)	41.2% (7.9%)	78.13% (0%)	49.6% (11.3%)	50.1% (12.5%)	79.7% (31.5%)
Projection uncertainty (IQR) > 1 m (2 m)	49.8% (4.9%)	36.0% (4.0%)	41.3% (6.4%)	43.6% (7.1%)	56.1% (24.5%)
Combined uncertainty > 1 m (2 m)	67.0% (22.1%)	100.0% (11.5%)	73.0% (27.9%)	75.0% (26.9%)	74.9% (48.9%)
Present-day uncertainty (IQR) > Projected absolute changes (Δ)	69.0%	85.0%	80.0%	79.0%	81.4%
Present-day uncertainty (IQR) > Projection uncertainty (IQR)	48.3%	69.0%	61.0%	58.8%	52.0%

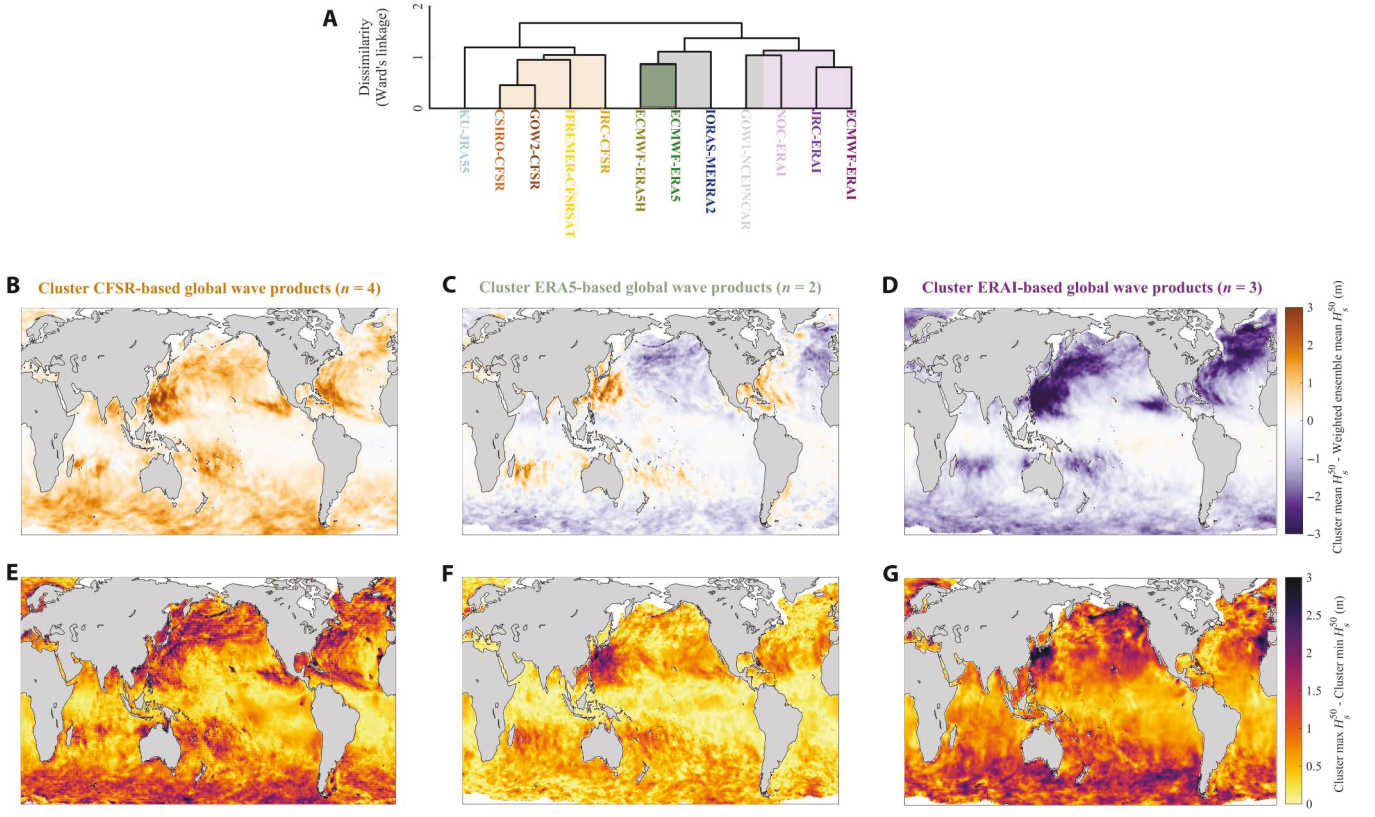

Fig. 3. Cluster analysis of H_s^{50} estimates obtained from global wave model products. (**A**) Cluster diagram (dendrogram) resulting from Euclidean distance–based Ward's minimum variance clustering using global pairwise H_s^{50} (Materials and Methods) with the vertical axis representing the distance or dissimilarity between clusters and cluster members presented as log scale for clarity. Shading represents defined clusters and subclusters. Note that gray shading on the cluster diagram represents subcluster(s) with different atmospheric forcing within one of the main clusters (**B** to **D**) Mean estimate of each cluster, or subcluster, based on the same atmospheric reanalysis, as per colors, minus the weighted ensemble mean. (**E** to **G**) Maximum difference between estimates within each respective cluster or subcluster.

from the selection of EVA model (here by comparing GEV-AMAX and GUM-AMAX) shows that the former dominates over the latter (almost everywhere) across the globe (fig. S10). We note, however, that we only considered two commonly used EVA methods within our analysis as previously discussed, and extending this analysis to sample more methods, such as *r*-largest, peak over threshold, and/or conditional average exceedance rate, could result in an increase in the EVA-related uncertainty (and exacerbate the combined uncertainties presented in this analysis).

Extreme value projections

So far, we analyzed present-day uncertainty associated with contemporary extreme H_s estimates from global wave reanalysis/hindcast products forced with atmospheric reanalysis winds. Next, we compare this uncertainty to projected future changes in extreme wave events and associated uncertainties due to global warming, obtained using statistical and dynamical wave simulations forced with climate model wind projections. To do this, and for consistency, we assess changes in H_s^n using AMAX H_s data extracted from the most comprehensive ensemble of global wave projections containing a total of 39 global wave simulations (*49*) developed for the high-risk representation concentration pathway RCP8.5 (Materials and Methods) (*50*). In contrast to past analyses, which calculated projected changes in extreme wave events based on single-method ensembles (*27*, *31*–*33*, *35*), our ensemble (*26*, *49*) covers different climate model, global climate models (GCM), forcing and wave-modeling methods, hence providing the most complete assessment of uncertainty to date (*49*). The projected future changes are obtained using a weighted multimember ensemble mean and its associated uncertainty (Fig. 4, C and D) quantified by bootstrapping the ensemble IQR (Materials and Methods). We find that H_s^{50} values are projected to increase by ~5 to 15% across the Southern Ocean, eastern Pacific Ocean, and northeastern Pacific Ocean and also across localized regions (e.g., Arabian Sea, Gulf of Bengal, Aleutian Sea, or China Sea). In contrast, there is a widespread projected decrease of up to −15% across the northern and central Atlantic Ocean, northwestern Pacific Ocean, Indian Ocean, and southern Pacific Ocean. In general, the overall spatial patterns of change in H_s^{50} shown are consistent with those of past analyses based on CMIP5-based dynamical wave ensembles (*27*, *33*).

When we compare the present-day uncertainties to projected changes for the 50-year event, we find that the former dominates over the latter across ~81% of the global ocean and ~79% of the coastline (Table 1 and Fig. 4E). The exceptions are localized tropical areas where the present-day uncertainty values are almost negligible (Fig. 4B) and a few particular areas within the Southern Ocean where projected future changes are large enough to exceed the present-day uncertainties (see fig. S4). In addition, we find that

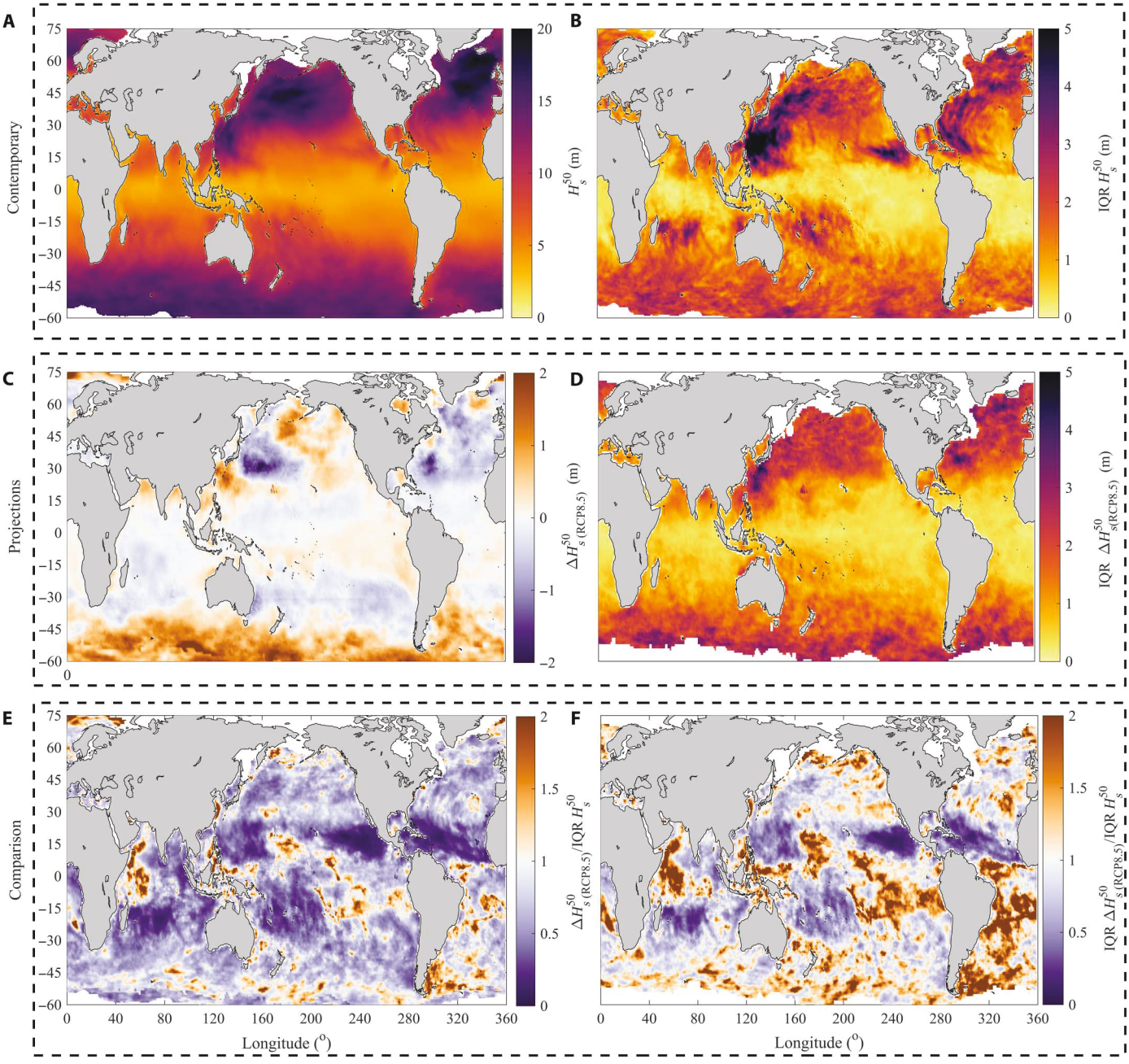

Fig. 4. Comparison of present-day uncertainty, projected future changes, and projection uncertainty for H_s^{50}. (**A**) Weighted ensemble mean of contemporary ensemble (hindcasts and reanalysis products) estimates (H_s^{50}). (**B**) Interquartile range (IQR) of contemporary ensemble (hindcasts and reanalysis products) estimates (IQR H_s^{50}). (**C**) Weighted ensemble mean of projected future changes ($\Delta H_{s\,RCP8.5}^{50}$) using climate model–driven wave simulations. (**D**) IQR of ensemble projections (IQR $\Delta H_{s\,RCP8.5}^{50}$). (**E**) Weighted ensemble mean (C)/(B) [and rather than weighted ensemble mean (C) over (B)]. (**F**) Weighted ensemble mean (D)/(B) [and rather than weighted ensemble mean (D) over (B)].

the present-day uncertainties exceed the uncertainties in the projections across ~52% of the global ocean area and ~59% of the coastline (Table 1). These areas are predominantly TC-dominated regions (Fig. 4F) but extend to specific extratropical areas (e.g., central-northern Atlantic Ocean, Southern Ocean, and southeastern Pacific Ocean) and to some localized regions (e.g., Gulf of Guinea). In all remaining regions, the uncertainties in the future projections exceed the present-day uncertainties.

The projected future changes and future uncertainties presented within regions directly affected by TC activity need to be considered carefully. We attribute the low ratio (<0.25) shown within TC-dominated regions (see Fig. 4, E and F) to the limited representation of intense TC systems within standard GCM simulations. So far, only a

few GCM-driven global wave simulations have been forced with atmospheric forcing high-resolution models (*51*), instead being forced with GCMs that tend to underestimate TC intensity and/or frequency due to their coarser resolutions (*52*). Therefore, most GCM-driven global wave simulations underestimate extreme H_s^n patterns produced by TC events (fig. S11) and cannot sufficiently resolve their potential future change due to global warming (*53*, *54*). In addition, although our ensemble of projections exhibits no robust (or statistically significant) changes in the shape of the underlying distribution (fig. S12) (*33*), GUM-AMAX usually underestimates TC-driven wave extremes (Materials and Methods), which are generally characterized by heavy-tailed distributions (fig. S9) and more adequately resolved using a "nonzero" shape distribution (such as GEV-AMAX). Now, there is no consensus on anthropogenic influences on major TC events (*55*) and TC-driven wave extremes—simulated using high-resolution atmospheric forcing (*53*, *54*). However, if proven that global warming could drive a significant increase in major TC events not resolved within existing simulations, then this could potentially affect the shape of the underlying distribution and make projected future changes and projection uncertainties potentially comparable, or even exceed, the present-day uncertainties within those TC areas (further exacerbating the combined uncertainties discussed within this analysis).

To further contextualize our findings, we present results at existing global offshore oil and gas platforms, offshore wind projects, and coastal seaports (see Fig. 5). Figure 5 (A and B) shows that present-day uncertainties for the 50-year events exceed projected future changes (dark and light orange marks), sometimes by more than 50% (dark orange marks), at more than ~70% of the infrastructure locations (Table 1). However, at 30% of the offshore and gas platform sites, projected changes exceed present-day uncertainties, highlighting that many existing infrastructure supporting the offshore energy production industry are at greater risk of being affected by changes in extreme waves due to global climate warming. Figure 5 (C and D) shows that present-day uncertainties exceed the uncertainties in global wave projections (purple and blue marks) at a significant percentage of infrastructure sites (48% of offshore oil and natural gas platforms, 69% of offshore wind farms, and 61% of open-coast seaports). The combined uncertainties are shown to be considerable at many sites (Fig. 4, C and D), exceeding more than 1 m (and 2 m) at 67% (22.1%) of the global offshore platform locations and 73% (27%) of coastal seaport sites (Table 1). Consistent with Fig. 4, we find that results have strong regional dependence. For example, most sites in Africa and South America exhibit a relatively low combined uncertainties (<1 m) (yet still dominated by present-day uncertainties), while sites in Europe and North America have relatively higher uncertainties (>2 to 3 m).

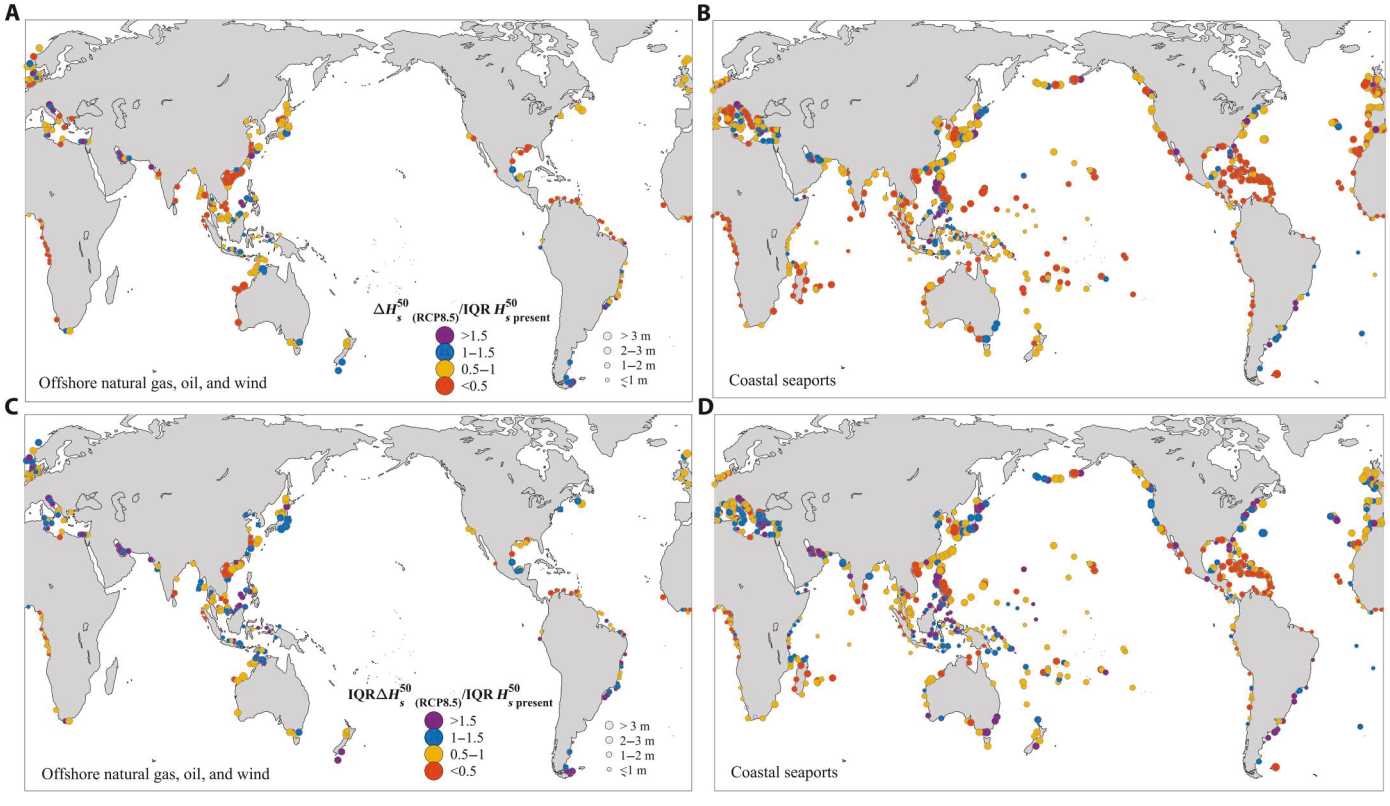

Fig. 5. Relative importance of present-day H_s^{50} uncertainties and projected H_s^{50} changes, and associated uncertainties, at existing offshore and coastal infrastructure locations. (**A**) Relative importance of projected absolute changes relative to present-day climate uncertainties at offshore oil and natural gas platforms (circles) and offshore wind farms (squares). (**B**) Relative importance of projected absolute changes relative to present-day climate uncertainties at open-coast sea ports. (**C**) Relative importance of projection uncertainty relative to present-day climate uncertainties at offshore oil and gas platforms (circles) and offshore wind farms (squares) and (**D**) relative importance of projection uncertainty relative to present-day uncertainties at open-coast sea ports. In all panels, combined uncertainties are indicated by the circle sizes according to the legends of (A) and (C).

DISCUSSION

Our analyses have shown large uncertainties associated with present-day extreme H_s^n estimates determined from many global wave products that are widely used for broad-scale offshore and coastal infrastructure design and hazard/risk assessments. Consequently, findings drawn from any single global wave product need to be treated carefully and/or contextualized. In addition to showing that atmospheric (reanalysis) forcing is the major driver of uncertainties in present-day extreme H_s^n estimates, our analysis also indicates that differences in global wave modeling methods can lead to significant discrepancies between present-day H_s^n estimates. This analysis also highlight that no individual product can represent the observational records across all wave buoy locations even within specific regions. Instead, within each region or basin with available buoy observations, some specific products lead to a more reliable representation of the regional buoy records than others.

Our analysis assesses projected changes in H_s^n using a large CMIP5-coordinated ensemble of wave projections across climate models and global wave modeling methods (*49*), thus allowing a much improved sampling of uncertainty relative to past analyses (*27*, *28*, *31*, *33*, *34*). We show that present-day extreme H_s^n uncertainties largely outpace climate-driven changes in H_s^n almost everywhere, even when considering a high-emission scenario (5°C warming by 2100) with no stringent climate mitigation (RCP8.5) (*50*). In addition, present-day H_s^n uncertainty levels are found to be comparable to and/or exceed the uncertainties associated with projected future H_s^n changes across widespread areas. These results suggest that present-day uncertainties are even more relevant when considering milder future warming climate scenarios (ranging 2° to 4°C) that consider stricter climate mitigation policies.

The uncertainties in present-day extreme H_s^n estimates shown have wide-reaching implications for structural designs loads, coastal erosion, and flooding. For example, although different wave setup parameterizations have been used (*18*, *19*, *56*), some large-scale coastal flood risk analyses simply approximate wave setup contribution as ~20% of offshore extreme H_s (*16*, *17*, *57*–*60*). On the basis of our results, which show that present-day H_s^{50} uncertainty owing to global wave model product differences can reach ~2.5 m when averaged across data offshore of coastal areas and up to 5 m at specific locations, this could lead to uncertainties of 0.5 m and up to 1 m at specific sites. This exceeds or is comparable to other uncertainties that are considered critical for current and future coastal hazard flooding and adaptation assessments (*22*), such as global tide-storm surge hindcast models, digital elevation model datasets, and sea level rise scenarios (*22*, *48*). For instance, contemporary extreme storm surge estimates (e.g., 100-year events) differ on average by 0.5 m, depending on the global hindcast model used (*48*). Although broad-scale assessments are now beginning to consider potential changes in extreme wave climate due to climate change (*16*–*19*), assessments to date have not accounted for present-day uncertainties in extreme wave events, which are essential to fully assess potential hazards and adaptation needs.

Expansion of the existing buoy networks and remote sensing datasets will improve assessment of extreme ocean wave events from global wave model products and potentially enhance future products (*13*, *61*). The Sofar network of globally distributed drifting surface weather buoys has expanded rapidly to more than 600 buoys (*62*). Maintaining such networks to enable climate relevant over time will provide data with greatly improved spatial resolution to complement the network of fixed observation platforms. Improving representation of TC and ETC systems within global atmospheric reanalyses with more data assimilation (*63*, *64*) and development of new globally downscaled atmospheric reanalysis data (*65*) would also help to further constrain uncertainties. Expanding the limited number of dynamical global wave simulations forced by high-resolution downscaled climate models (0.25° or less) that are more capable of resolving TC-driven waves (relative to coarse CMIP-driven global wave simulations) (*53*, *54*) might also help to understand and reduce uncertainties in ETC and TC areas. As previously discussed, our community-based ensemble of global wave projections [and any other ensembles based on standard GCM model data; see (*27*, *31*–*34*)] may not sufficiently represent potential future TC changes, suggesting that further research on TC projections and regional-scale TC-produced ocean wave extremes (e.g., using regional high-resolution GCMs and regional synthetic TC events) is needed.

In conclusion, we highlight that present-day uncertainties in extreme wave height derived from the existing ensemble of global wave hindcasts/reanalysis exceed and/or are comparable to that of global wave model projections (and associated uncertainties). Hence, uncertainties inherent to both future projections and present-day estimates need to be accounted for and combined in comprehensive offshore and coastal risk assessments relying on extreme wave data. Otherwise, incorporating ongoing improvements in climate modeling without addressing uncertainties in the wave climate system may provide little benefit for many broad-scale impact and adaptation assessments.

MATERIALS AND METHODS

Contemporary global wave reanalysis and hindcasts

AMAX H_s data were taken from the first coordinated multiproduct ensemble of global wave reanalysis/hindcast product (*37*). This recently assembled dataset was compiled under a standardized research framework (*37*) and provides general and extreme wave statistics (including AMAX H_s calculated from sub-daily time series) for 14 global wave products produced using third-, fourth-, and fifth-generation atmospheric reanalyses as forcing (*37*). In this analysis, we use all the global wave products (two reanalysis and nine hindcasts) that cover the full temporal record length available of 35 years (between 1980 and 2014) (*37*). To further expand our sampling space, we also included a JRA55-forced global wave hindcast (KU-JRA55) that spans 32 years (between 1980 and 2012). The full description of all global wave product datasets (including their validation) is extensively provided elsewhere (*37*), and hence, we only provide a brief summary of their key characteristics along with respective acronyms (table S1).

Global wave buoy measurements

In situ wave buoy stations with long-term data records are relatively scarce worldwide. Hence, wave buoy selection was based on a compromise between buoy availability and data suitability. We used time series of AMAX H_s calculated from (hourly to 3-hourly) measurements extracted from all available wave buoy record networks that meet a number of previously adopted quality requirements (*33*) to ensure robust estimates and a suitable comparison against

reanalysis and hindcasts across a maximum number of suitable locations. We used all buoy stations that are: (i) moored at water depths of less than 45 m to ensure that ocean waves are not heavily affected to shallow-water nonlinear processes unresolved by current global wave models; (ii) sufficiently far from land so that corresponding wave model output data are located at sea; and (iii) resultant time series of AMAX H_s must comprise at least 20 values chosen on the basis of (*33*): (i) AMAX values for buoys sited above 40°N or below 40°S (extratropical region) are selected from all years with >60% of sub-daily data available during boreal (January, February, and December) and austral (June, July, and August) winter seasons (respectively), and (ii) AMAX values for buoys located below 40°N or above 40°S (subtropical and tropical regions) are selected from all years with >60% of sub-daily data available. In total, we assembled a network of 64 wave buoys, which we use to estimate H_s^n (fig. S1 and table S2).

Comparison against model estimates

The global wave model products used provide continuous time series of AMAX H_s for 35 years (see "Contemporary global wave reanalysis and hindcasts" section). Nonetheless, our quality-controlled buoy records are often shorter (table S2). Therefore, to provide a coherent comparison between H_s^n estimated from model and buoys, we removed any years from product time series of AM data that are missing within the observational records when comparing buoys and models (while always ensuring a 20-year record length) before calculating return periods.

Statistical extreme value models

Applying EVA approaches to observed (or modeled) extreme H_s data allows the quantification of return periods that are longer than available records (*38*, *39*). Now, there is an existing range of statistical EVA methods that can be used to derive H_s^n (*38*). Although specific methods could be favored when certain criteria are fulfilled (e.g., sufficient data length and availability of sub-daily data), there is no universally accepted standard method for extreme wave analysis (*21*, *38*). Two reference extreme value distributions (GEV and GUM maxima) have been widely used to estimate H_s^n from AMAX series (*33*, *34*) and are used here

$$H_{s\,\mathrm{GEV-AMAX}}^{n} = \mu - \frac{\sigma}{k}\left(1 - \left\{-\log\left(1 - \frac{1}{n}\right)\right\}^{-k}\right) \quad (1)$$

where μ is the location parameter, σ is the scale parameter, and k is the shape parameter, with $k > 1$ representing a heavy-tailed distribution (Fréchet family) and $k < 1$ representing a bounded upper limit–tailed distribution (Weibull family). The GUM (maxima) distribution assumes that $k = 0$ and represents a two-parameter light tailed distribution

$$H_{s\,\mathrm{GUM-AMAX}}^{n} = \mu - \sigma\,\log\left\{-\log\left(1 - \frac{1}{n}\right)\right\} \quad (2)$$

In this analysis, we assumed a conservative approach and constrain estimates to 50-year return events (H_s^{50}) to prevent unreliable extrapolation periods. In all cases, the statistical distribution parameters were calculated using the asymptotically optimal maximum likelihood estimator. Alternative parameter estimation methods exist (e.g., method of moments or L-moments), but we have not considered them because their influence would be insignificant relative to the key uncertainties discussed.

Suitability of underlying data and statistical model fit

To have a consistent comparison of the different uncertainties across the global ocean, the same extreme value distribution must be adopted (*33*, *66*). There is a range of accepted methods that can be used to assess how well extreme value models fit a given climate dataset. We compared the suitability and the fit of GEV-AMAX and GUM-AMAX using different methods.

Anderson-Darling statistical test

We used the Anderson-Darling test (*67*) at 5% confidence level to determine whether the time series of AMAX H_s follow a GUM distribution (our null hypothesis) versus any other (extreme) distribution. The results show that the null hypothesis is not rejected (i.e., there is no significant departure from the GUM distribution) across more than ~85% of the global ocean regardless of the global wave model product used (fig. S13). The regions where the null hypothesis is rejected ($P < 0.05$) are limited to specific TC dominated as explained below.

Significance of shape parameter fit

We assessed the statistical significance of the fit of the GEV-AMAX shape parameter k at 95% confidence level using its estimated confidence limits. The results show that the fit of k is not statistically significant from zero across more than ~85% of the global ocean (fig. S9). The areas where k is found to provide a significant fit (less than 15%) (fig. S9) are specific TC-dominated areas, typically characterized by heavy-tailed distributions, where the suitability of the GUM distribution is compromised on the basis of the Anderson-Darling test (fig. S13). These results are consistent with previous global-scale analyses (*33*), which used GUM-AMAX after showing that such model provides an overall more suitable fit compared to GEV-AMAX when applied to global wave hindcast data (GOW2) and CMIP5-driven global wave simulations.

Akaike information criterion

To further support our results, we determined the Akaike information criterion (corrected for small samples) (AICc) (*68*) for both GUM-AMAX and GEV-AMAX. The AICc is an estimator of prediction error used across different scientific research fields (*69*, *70*), which asymptotically selects the extreme value distribution that minimizes the mean squared errors of the estimation. The AIC corrected for small sample sizes ($N/W < 40$) is provided by

$$\mathrm{AICc} = -2\log L(\hat{\theta}) + 2W + \frac{2W(W+1)}{N - W - 1} \quad (3)$$

with $L(\hat{\theta})$ representing the maximized log-likelihood, W representing the number of estimated parameters used to achieve that log-likelihood, and N representing the sample size. The AICc is calculated on the basis of a compromise between goodness of fit and model complexity with lower AICc values indicating a better-fit model. The results are provided in fig. S14.

Bayesian information criterion

We also determined the Bayesian information criterion (BIC)

$$\mathrm{BIC} = -2\log L(\hat{\theta}) + W\log(N) \quad (4)$$

which selects the model that maximizes the posterior model probability. The comparison of the AICc and BIC values for GUM-

AMAX and GEV-AMAX shows that GUM-AMAX provides a better-fit model across 70 to 78% and 78 to 86% of the global ocean, respectively (depending on the global wave product used) (figs. S14 and S15). The only areas where GEV-AMAX lends a better-fit model correspond to specific TC-dominated regions (less than 15 to 20%) where GUM-AMAX could result in an underestimation of heavy-tailed distributions (and associated estimates). These results (combined with the fact that our ensemble projections of k exhibit no robust or statistically significance changes over most of the global ocean) support using GUM-AMAX as reference in this analysis, consistent with previous research (*33*).

Clustering methodology

We used an agglomerative hierarchical clustering analysis, with the similarity criterion defined by Ward's analysis of variance (ANOVA)–based minimum variance algorithm (*71*). The clustering method was used without imposing any restrictions on the number and size or any a priori assumptions of clusters. The initial cluster distances (used within the Ward's minimum variance method) were obtained using a multidimensional approach, where the pairwise Euclidean distance (D) among model products is derived at every grid node, rather than spatially averaged, thus clustering products with high similarity regarding spatial pattern and magnitude (*26*)

$$D_{i,j,k} = \sqrt{\sum_{k=1}^{w} (x_{i,k} - x_{j,k})^2} \quad (5)$$

where $x_{i,k}$ and $x_{j,k}$ are the H_s^{50} estimates derived from two given global wave products i and j, respectively, at grid point k with w equal to the number of ocean grid nodes. We tested alternative clustering distance metrics and obtained consistent results.

Weighted ensemble mean of global wave hindcasts and reanalyses

The findings of our skill analysis (figs. S2 and S3), along with the sparsity of global wave buoys records (fig. S1), preclude weighting individual ensemble models based on their relative skill. Nevertheless, we show that present-day H_s^n estimates are strongly dependent on reanalysis forcing (fig. S3), and therefore, a weighted multiproduct ensemble mean was calculated by applying weighting factor to each global wave product

$$\overline{H_{s\,k}^n} = \frac{\sum_{v=1}^{12} (H_{s\,v,k}^n \times W_{v,k})}{\sum_{v=1}^{12} W_{v,k}} \quad (6)$$

where $H_{s\,v,k}^n$ represents the estimate of H_s^n according to the ensemble model product v at each grid point k and $WT_{j,k}$ its weighting factor representing the number of ensemble products with that same atmospheric reanalysis forcing among all products available.

Global wave model projections

Time series of AMAX H_s were taken from the largest ensemble of CMIP5-based global ocean wave projections available to date (spanning different global climate model forcings and global wave downscaling methods) (table S3). This ensemble and its members have been extensively described and validated (*26*, *37*). The data were extracted over two available representative time slices: a reference historical period (1980 to 2005) and a future climate period (2080 to 2100) that assumes a high-end warming scenario (RCP8.5). In total, AMAX H_s extracted from 38 simulations were used to estimate projected future changes and associated uncertainties.

Calculation of projected future changes

The projected relative change in H_s^n was calculated as percentage change (and absolute change) for each ensemble model member following (*26*)

$$\Delta H_{s\,k}^n = \frac{(H_{s\,j,k}^{n\,\mathrm{Future}} - H_{s\,j,k}^{n\,\mathrm{Present}})}{H_{s\,j,k}^{n\,\mathrm{Present}}} \quad (7)$$

where $\Delta H_{s\,j,k}^n$ represents the projected future changes according to the ensemble member j at each grid point k. We determined a weighted multimember ensemble mean of projected future change by applying weighting factors to each ensemble member (table S3) on the basis that projected changes are strongly dependent on climate model forcing (*26*, *72*)

$$\overline{\Delta H_{s\,k}^n} = \frac{\sum_{j=1}^{39} (\Delta H_{s\,j,k}^n \times W_{j,k})}{\sum_{j=1}^{39} W_{j,k}} \quad (8)$$

where $W_{j,k}$ is the weighting factor for the ensemble model member j, calculated as the number of ensemble members with that same climate model forcing among all members available.

Calculation of uncertainty

Present-day uncertainty

The uncertainty associated with using different global wave reanalysis/hindcast products (here, present-day uncertainty) is calculated using the IQR of the entire ensemble estimates of H_s^n (Fig. 4B). The IQR is considered to be the most suitable measure of variability for nonnormal or skewed data distributions and/or datasets with outliers. We also calculate the max-min difference between ensemble estimates, and the results are consistent (fig. S6).

Projection uncertainty

For consistency, the uncertainty related to global extreme wave projections (future uncertainty) is calculated using the IQR of the projected change estimates in H_s^n from the different members. In this case, we apply a bootstrapping procedure to the IQR values (i.e., we subsampled 12 ensemble members at the time, for 1000 times, and calculated the mean of the 1000 IQR values) to match the number of samples when comparing the present-day and future uncertainties. The results are consistent with those obtained without applying any bootstrapping.

Combined uncertainty

The different uncertainties discussed (that is, IQRs associated with contemporary H_s^n estimates and those associated with global projections of extreme waves) are here combined using the root of the sum of their respective IQR values as follows

$$\mathrm{Combined}_{\mathrm{IQR}} = \sqrt{\sum_{j}^{N=2} (\mathrm{IQR}_j)^2} \quad (9)$$

where N is the number of individual uncertainties (here, $N = 2$) that are being combined.

Offshore and coastal infrastructure data

The exact locations of the offshore wind farm projects were extracted from a publicly available global remote sensing–based offshore wind turbine database obtained from Sentinel-1 synthetic aperture radar extensively validated time-series images (*73*). Because the dataset contains all the existing wind turbines deployed, we considered each aggregation of turbines as a single farm project based on their central coordinates (*73*). The locations of the global deep offshore oil and natural gas platforms were extracted from a global dataset that was published as part of a global analysis of the projected footprint of marine-built structures (*9*). The global open-coast seaports were obtained from a published global-scale analysis (*74*) based on a refined version of the World Port Index database (provided by the National Geospatial-Intelligence Agency).

Supplementary Materials

This PDF file includes:

Supplementary Information
Figs. S1 to S16
Tables S1 and S2
References

REFERENCES AND NOTES

1. P. L. Barnard, A. D. Short, M. D. Harley, K. D. Splinter, S. Vitousek, I. L. Turner, J. Allan, M. Banno, K. R. Bryan, A. Doria, J. E. Hansen, S. Kato, Y. Kuriyama, E. Randall-Goodwin, P. Ruggiero, I. J. Walker, D. K. Heathfield, Coastal vulnerability across the Pacific dominated by El Niño/Southern Oscillation. *Nat. Geosci.* **8**, 801–807 (2015).
2. N. Leonardi, N. Ganju, S. Fagherazzi, A linear relationship between wave power and erosion determines salt-marsh resilience to violent storms and hurricanes. *Proc. Natl. Acad. Sci. U.S.A.* **113**, 64–68 (2015).
3. A. Melet, B. Meyssignac, R. Almar, G. Le Cozannet, Under-estimated wave contribution to coastal sea-level rise. *Nat. Clim. Change* **8**, 234–239 (2018).
4. C. Storlazzi, S. B. Gingerich, A. van Dongeren, O. M. Cheriton, P. W. Swarzenski, E. Quataert, C. I. Voss, D. W. Field, H. Annamalai, G. A. Piniak, R. M. Call, Most atolls will be uninhabitable by the mid-21st century because of sea-level rise exacerbating wave-driven flooding. *Sci. Adv.* **4**, eaap9741 (2018).
5. K. A. Serafin, P. Ruggiero, H. F. Stockdon, The relative contribution of waves, tides, and nontidal residuals to extreme total water levels on U.S. West Coast sandy beaches. *Geophys. Res. Lett.* **44**, 1839–1847 (2017).
6. Z. Zhang, X.-M. Li, Global ship accidents and ocean swell-related sea states. *Nat. Hazards Earth Syst. Sci.* **17**, 2041–2051 (2017).
7. DNVGL, "Offshore standards DNVGL-OS-C201 - Structural design of offshore units" (2016).
8. ISO/TC 67/SC 7 Offshore structures, "ISO 19901-1:2015 Petroleum and natural gas industries — Specific requirements for offshore structures — Part 1: Metocean design and operating considerations" (2015).
9. A. B. Bugnot, M. Mayer-Pinto, L. Airoldi, E. C. Heery, E. L. Johnston, L. P. Critchley, E. M. A. Strain, R. L. Morris, L. H. L. Loke, M. J. Bishop, E. V. Sheehan, R. A. Coleman, K. A. Dafforn, Current and projected global extent of marine built structures. *Nat. Sustain.* **4**, 33–41 (2021).
10. S. Gourvenec, F. Sturt, E. Reid, F. Trigos, Global assessment of historical, current and forecast ocean energy infrastructure: Implications for marine space planning, sustainable design and end-of-engineered-life management. *Renew. Sustain. Energy Rev.* **154**, 111794 (2022).
11. A. Toimil, I. J. Losada, R. J. Nicholls, R. A. Dalrymple, M. J. F. Stive, Addressing the challenges of climate change risks and adaptation in coastal areas: A review. *Coast. Eng.* **156**, 103611 (2020).
12. A. J. Dowdy, G. A. Mills, B. Timbal, Y. Wang, Fewer large waves projected for eastern Australia due to decreasing storminess. *Nat. Clim. Change* **4**, 283–286 (2014).
13. F. Ardhuin, J. E. Stopa, B. Chapron, F. Collard, R. Husson, R. E. Jensen, J. Johannessen, A. Mouche, M. Passaro, G. D. Quartly, V. Swail, I. Young, Observing sea states. *Front. Mar. Sci.* **6**, 124 (2019).
14. J. P. Sierra, M. Casas-Prat, Analysis of potential impacts on coastal areas due to changes in wave conditions. *Clim. Change* **124**, 861–876 (2014).
15. DNVGL, "Class Guideline DNVGL-CG-0130 - Wave loads" (2018).
16. R. Almar, R. Ranasinghe, E. W. J. Bergsma, H. Diaz, A. Melet, F. Papa, M. Vousdoukas, P. Athanasiou, O. Dada, L. P. Almeida, E. Kestenare, A global analysis of extreme coastal water levels with implications for potential coastal overtopping. *Nat. Commun.* **12**, 3775 (2021).
17. M. I. Vousdoukas, L. Mentaschi, E. Voukouvalas, M. Verlaan, S. Jevrejeva, L. P. Jackson, L. Feyen, Global probabilistic projections of extreme sea levels show intensification of coastal flood hazard. *Nat. Commun.* **9**, 2360 (2018).
18. S. Vitousek, P. L. Barnard, C. H. Fletcher, N. Frazer, L. H. Erikson, C. D. Storlazzi, Doubling of coastal flooding frequency within decades due to sea-level rise. *Sci. Rep.* **7**, 1399 (2017).
19. E. Kirezci, I. R. Young, R. Ranasinghe, S. Muis, R. J. Nicholls, D. Lincke, J. Hinkel, Projections of global-scale extreme sea levels and resulting episodic coastal flooding over the 21st century. *Sci. Rep.* **10**, 11629 (2020).
20. J. B. Shope, L. H. Erikson, P. L. Barnard, C. D. Storlazzi, K. Serafin, K. Doran, H. Stockdon, B. Reguero, F. Mendez, S. Castanedo, A. Cid, L. Cagigal, P. Ruggiero, Characterizing storm-induced coastal change hazards along the United States West Coast. *Sci. Data* **9**, 224 (2022).
21. S. Caires, A. Sterl, 100-Year return value estimates for ocean wind speed and significant wave height from the ERA-40 data. *J. Climate* **18**, 1032–1048 (2005).
22. J. Hinkel, L. Feyen, M. Hemer, G. Le Cozannet, D. Lincke, M. Marcos, L. Mentaschi, J. L. Merkens, H. de Moel, S. Muis, R. J. Nicholls, A. T. Vafeidis, R. S. W. van de Wal, M. I. Vousdoukas, T. Wahl, P. J. Ward, C. Wolff, Uncertainty and bias in global to regional scale assessments of current and future coastal flood risk. *Earth's Future* **9**, e2020EF001882 (2021).
23. J. E. Stopa, K. F. Cheung, Intercomparison of wind and wave data from the ECMWF reanalysis interim and the NCEP Climate Forecast System Reanalysis. *Ocean Model.* **75**, 65–83 (2014).
24. J. E. Stopa, F. Ardhuin, A. Babanin, S. Zieger, Comparison and validation of physical wave parameterizations in spectral wave models. *Ocean Model.* **103**, 2–17 (2016).
25. V. D. Sharmar, M. Y. Markina, S. K. Gulev, Global ocean wind-wave model hindcasts forced by different reanalyzes: A comparative assessment. *J. Geophys. Res. Oceans* **126**, e2020JC016710 (2021).
26. J. Morim, M. Hemer, X. L. Wang, N. Cartwright, C. Trenham, A. Semedo, I. Young, L. Bricheno, P. Camus, M. Casas-Prat, L. Erikson, L. Mentaschi, N. Mori, T. Shimura, B. Timmermans, O. Aarnes, Ø. Breivik, A. Behrens, M. Dobrynin, M. Menendez, J. Staneva, M. Wehner, J. Wolf, B. Kamranzad, A. Webb, J. Stopa, F. Andutta, Robustness and uncertainties in global multivariate wind-wave climate projections. *Nat. Clim. Change* **9**, 711–718 (2019).
27. A. Meucci, I. R. Young, M. Hemer, K. Ebru, R. Roshanka, Projected 21st century changes in extreme wind-wave events. *Sci. Adv.* **6**, eaaz7295 (2020).
28. L. Mentaschi, M. I. Vousdoukas, E. Voukouvalas, A. Dosio, L. Feyen, Global changes of extreme coastal wave energy fluxes triggered by intensified teleconnection patterns. *Geophys. Res. Lett.* **44**, 2416–2426 (2017).
29. L. M. Bricheno, J. Wolf, Future wave conditions of Europe, in response to high-end climate change scenarios. *J. Geophys. Res. Oceans* **123**, 8762–8791 (2018).
30. M. Casas-Prat, X. L. Wang, Projections of extreme ocean waves in the arctic and potential implications for coastal inundation and erosion. *J. Geophys. Res. Oceans* **125**, e2019JC015745 (2020).
31. A. Patra, S.-K. Min, P. Kumar, X. L. Wang, Changes in extreme ocean wave heights under 1.5 °C, 2 °C, and 3 °C global warming. *Weather Clim. Extremes* **33**, 100358 (2021).
32. X. L. Wang, Y. Feng, V. R. Swail, Changes in global ocean wave heights as projected using multimodel CMIP5 simulations. *Geophys. Res. Lett.* **41**, 1026–1034 (2014).
33. H. Lobeto, M. Menendez, I. J. Losada, Future behavior of wind wave extremes due to climate change. *Sci. Rep.* **11**, 7869 (2021).
34. J. G. O'Grady, M. A. Hemer, K. L. McInnes, C. E. Trenham, A. G. Stephenson, Projected incremental changes to extreme wind-driven wave heights for the twenty-first century. *Sci. Rep.* **11**, 8826 (2021).
35. J. Morim, M. Hemer, N. Cartwright, D. Strauss, F. Andutta, On the concordance of 21st century wind-wave climate projections. *Glob. Planet. Change* **167**, 160–171 (2018).
36. M. Collins, M. Sutherland, L. Bouwer, S.-M. Cheong, T. Frölicher, H. Jacot Des Combes, M. Koll Roxy, I. Losada, K. McInnes, B. Ratter, E. Rivera-Arriaga, R. D. Susanto, D. Swingedouw, L. Tibig, Extremes, abrupt changes and managing risk, in *IPCC Special Report on the Ocean and Cryosphere in a Changing Climate* (Cambridge University Press, 2019), pp. 589–655. https://doi.org/10.1017/9781009157964.008.

37. J. Morim, L. H. Erikson, M. Hemer, I. Young, X. Wang, N. Mori, T. Shimura, J. Stopa, C. Trenham, L. Mentaschi, S. Gulev, V. D. Sharmar, L. Bricheno, J. Wolf, O. Aarnes, J. Perez, J. Bidlot, A. Semedo, B. Reguero, T. Wahl, A global ensemble of ocean wave climate statistics from contemporary wave reanalysis and hindcasts. *Sci. Data* **9**, 358 (2022).
38. E. Vanem, Uncertainties in extreme value modelling of wave data in a climate change perspective. *J. Ocean Eng. Mar. Energy.* **1**, 339–359 (2015).
39. S. Coles, *An Introduction to Statistical Modeling of Extreme Values* (Springer Series in Statistics book series (SSS), 2001).
40. S. Caires, "JCOMM Technical Report No. 57 - Extreme value analysis: Wave data" (2011).
41. R. M. Campos, J. H. G. M. Alves, C. Guedes Soares, L. G. Guimaraes, C. E. Parente, Extreme wind-wave modeling and analysis in the south Atlantic ocean. *Ocean Model.* **124**, 75–93 (2018).
42. A. Meucci, I. R. Young, Ø. Breivik, Wind and wave extremes from atmosphere and wave model ensembles. *J. Climate* **31**, 8819–8842 (2018).
43. K. Hodges, A. Cobb, P. L. Vidale, How well are tropical cyclones represented in reanalysis datasets? *J. Climate* **30**, 5243–5264 (2017).
44. M. Rohrer, S. Brönnimann, O. Martius, C. C. Raible, M. Wild, G. P. Compo, Representation of extratropical cyclones, blocking anticyclones, and alpine circulation types in multiple reanalyses and model simulations. *J. Climate* **31**, 3009–3031 (2018).
45. Z. S. Aarons, S. J. Camargo, J. D. O. Strong, H. Murakami, Tropical cyclone characteristics in the MERRA-2 reanalysis and AMIP simulations. *Earth Space Sci.* **8**, e2020EA001415 (2021).
46. G.-F. Bian, G.-Z. Nie, X. Qiu, How well is outer tropical cyclone size represented in the ERA5 reanalysis dataset? *Atmos. Res.* **249**, 105339 (2021).
47. K. I. Hodges, R. W. Lee, L. Bengtsson, A comparison of extratropical cyclones in recent reanalyses ERA-Interim, NASA MERRA, NCEP CFSR, and JRA-25. *J. Climate* **24**, 4888–4906 (2011).
48. T. Wahl, I. D. Haigh, R. J. Nicholls, A. Arns, S. Dangendorf, J. Hinkel, A. B. A. Slangen, Understanding extreme sea levels for broad-scale coastal impact and adaptation analysis. *Nat. Commun.* **8**, 16075 (2017).
49. J. Morim, C. Trenham, M. Hemer, X. L. Wang, N. Mori, M. Casas-Prat, A. Semedo, T. Shimura, B. Timmermans, P. Camus, L. Bricheno, L. Mentaschi, M. Dobrynin, Y. Feng, L. Erikson, A global ensemble of ocean wave climate projections from CMIP5-driven models. *Sci. Data* **7**, 105 (2020).
50. Z. Hausfather, G. P. Peters, Emissions – The 'business as usual' story is misleading. *Nature* **577**, 618–620 (2020).
51. R. J. Haarsma, M. J. Roberts, P. L. Vidale, C. A. Senior, A. Bellucci, Q. Bao, P. Chang, S. Corti, N. S. Fučkar, V. Guemas, J. von Hardenberg, W. Hazeleger, C. Kodama, T. Koenigk, L. R. Leung, J. Lu, J.-J. Luo, J. Mao, M. S. Mizielinski, R. Mizuta, P. Nobre, M. Satoh, E. Scoccimarro, T. Semmler, J. Small, J.-S. von Storch, High resolution model intercomparison project (HighResMIP v1.0) for CMIP6. *Geosci. Model Dev.* **9**, 4185–4208 (2016).
52. S. J. Camargo, Global and regional aspects of tropical cyclone activity in the CMIP5 models. *J. Climate* **26**, 9880–9902 (2013).
53. T. Shimura, N. Mori, H. Mase, Future projections of extreme ocean wave climates and the relation to tropical cyclones: Ensemble experiments of MRI-AGCM3.2H. *J. Climate* **28**, 9838–9856 (2015).
54. B. Timmermans, D. Stone, M. Wehner, H. Krishnan, Impact of tropical cyclones on modeled extreme wind-wave climate. *Geophys. Res. Lett.* **44**, 1393–1401 (2017).
55. C. M. Patricola, M. F. Wehner, Anthropogenic influences on major tropical cyclone events. *Nature* **563**, 339–346 (2018).
56. R. K. Hoeke, K. L. McInnes, J. C. Kruger, R. J. McNaught, J. R. Hunter, S. G. Smithers, Widespread inundation of Pacific islands triggered by distant-source wind-waves. *Glob. Planet. Change* **108**, 128–138 (2013).
57. M. Marcos, J. Rohmer, M. I. Vousdoukas, L. Mentaschi, G. le Cozannet, A. Amores, Increased extreme coastal water levels due to the combined action of storm surges and wind waves. *Geophys. Res. Lett.* **46**, 4356–4364 (2019).
58. M. I. Vousdoukas, J. Clarke, R. Ranasinghe, L. Reimann, N. Khalaf, T. M. Duong, B. Ouweneel, S. Sabour, C. E. Iles, C. H. Trisos, L. Feyen, L. Mentaschi, N. P. Simpson, African heritage sites threatened as sea-level rise accelerates. *Nat. Clim. Change* **12**, 256–262 (2022).
59. M. I. Vousdoukas, L. Mentaschi, E. Voukouvalas, M. Verlaan, L. Feyen, Extreme sea levels on the rise along Europe's coasts. *Earth's Future* **5**, 304–323 (2017).
60. G. Dodet, A. Melet, F. Ardhuin, X. Bertin, D. Idier, R. Almar, The contribution of wind-generated waves to coastal sea-level changes. *Surv. Geophys.* **40**, 1563–1601 (2019).
61. I. A. Houghton, C. Hegermiller, C. Teicheira, P. B. Smit, Operational assimilation of spectral wave data from the Sofar Spotter network. *Geophys. Res. Lett.* **49**, e2022GL098973 (2022).
62. J. E. Stopa, Wind forcing calibration and wave hindcast comparison using multiple reanalysis and merged satellite wind datasets. *Ocean Model.* **127**, 55–69 (2018).
63. W. Sasaki, Impact of satellite data assimilation in atmospheric reanalysis on the marine wind and wave climate. *J. Climate* **29**, 6351–6361 (2016).
64. P. Malakar, A. P. Kesarkar, J. Bhate, A. Deshamukhya, Appraisal of data assimilation techniques for dynamical downscaling of the structure and intensity of tropical cyclones. *Earth Space Sci.* **7**, e2019EA000945 (2020).
65. J.-E. Kim, S.-Y. Hong, A global atmospheric analysis dataset downscaled from the NCEP–DOE reanalysis. *J. Climate* **25**, 2527–2534 (2012).
66. S. Muis, M. Verlaan, H. C. Winsemius, J. C. J. H. Aerts, P. J. Ward, A global reanalysis of storm surges and extreme sea levels. *Nat. Commun.* **7**, 11969 (2016).
67. T. W. Anderson, D. A. Darling, A test of goodness of fit. *J. Am. Stat. Assoc.* **49**, 765–769 (1954).
68. H. Akaike, Canonical correlation analysis of time series and the use of an information criterion, in *Mathematics in Science and Engineering*, R. K. Mehra, D. G. Lainiotis, Eds. (Elsevier, 1976), vol. 126, pp. 27–96. www.sciencedirect.com/science/article/pii/S0076539208608693.
69. F. J. Méndez, M. Menéndez, A. Luceño, I. J. Losada, Analyzing monthly extreme sea levels with a time-dependent GEV model. *J. Atmos. Oceanic Tech.* **24**, 894–911 (2007).
70. J. G. O'Grady, A. G. Stephenson, K. L. McInnes, Gauging mixed climate extreme value distributions in tropical cyclone regions. *Sci. Rep.* **12**, 4626 (2022).
71. B. S. Everitt, *Cluster Analysis* (Wiley Series in Probability and Statistics, ed. 5, 2011).
72. J. Morim, S. Vitousek, M. Hemer, B. Reguero, L. Erikson, M. Casas-Prat, X. L. Wang, A. Semedo, N. Mori, T. Shimura, L. Mentaschi, B. Timmermans, Global-scale changes to extreme ocean wave events due to anthropogenic warming. *Environ. Res. Lett.* **16**, 074056 (2021).
73. T. Zhang, B. Tian, D. Sengupta, L. Zhang, Y. Si, Global offshore wind turbine dataset. *Sci. Data* **8**, 191 (2021).
74. C. Izaguirre, I. J. Losada, P. Camus, J. L. Vigh, V. Stenek, Climate change risk to global port operations. *Nat. Clim. Change* **11**, 14–20 (2021).
75. B. G. Reguero, M. Menéndez, F. Méndez, R. Mínguez, I. Losada, A global ocean wave (GOW) calibrated reanalysis from 1948 onwards. *Coast. Eng.* **65**, 38–55 (2012).
76. G. A. Smith, M. Hemer, D. Greenslade, C. Trenham, S. Zieger, T. Durrant, Global wave hindcast with Australian and Pacific Island focus: From past to present. *Geosci. Data J.* **8**, 24–33 (2021).
77. J. Perez, M. Menendez, I. Losada, GOW2: A global wave hindcast for coastal applications. *Coast. Eng.* **124**, 1–11 (2017).
78. J. E. Stopa, F. Ardhuin, E. Stutzmann, T. Lecocq, Sea state trends and variability: Consistency between models, altimeters, buoys, and seismic data (1979–2016). *J. Geophys. Res. Oceans* **124**, 3923–3940 (2019).
79. B. W. Timmermans, C. P. Gommenginger, G. Dodet, J.-R. Bidlot, Global wave height trends and variability from new multimission satellite altimeter products, reanalyses, and wave buoys. *Geophys. Res. Lett.* **47**, e2019GL086880 (2020).
80. J.-R. Bidlot, G. Lemos, A. Semedo, *2nd International Workshop on Waves, Storm Surges, and Coastal Hazards incorporating 16th International Workshop on Wave Hindcasting and Forecasting (2019)*, Melbourne, Australia, 10 to 15 November 2019.
81. T. Shimura, N. Mori, High-resolution wave climate hindcast around Japan and its spectral representation. *Coast. Eng.* **151**, 1–9 (2019).
82. D. P. Dee, S. M. Uppala, A. J. Simmons, P. Berrisford, P. Poli, S. Kobayashi, U. Andrae, M. A. Balmaseda, G. Balsamo, P. Bauer, P. Bechtold, A. C. M. Beljaars, L. van de Berg, J. Bidlot, N. Bormann, C. Delsol, R. Dragani, M. Fuentes, A. J. Geer, L. Haimberger, S. B. Healy, H. Hersbach, E. V. Hólm, L. Isaksen, P. Kållberg, M. Köhler, M. Matricardi, A. P. M. Nally, B. M. Monge-Sanz, J.-J. Morcrette, B.-K. Park, C. Peubey, P. de Rosnay, C. Tavolato, J.-N. Thépaut, F. Vitart, The ERA-Interim reanalysis: Configuration and performance of the data assimilation system. *Q. J. Roy. Meteorol. Soc.* **137**, 553–597 (2011).
83. H. Hersbach, B. Bell, P. Berrisford, S. Hirahara, A. Horányi, J. Muñoz-Sabater, J. Nicolas, C. Peubey, R. Radu, D. Schepers, A. Simmons, C. Soci, S. Abdalla, X. Abellan, G. Balsamo, P. Bechtold, G. Biavati, J. Bidlot, M. Bonavita, G. De Chiara, P. Dahlgren, D. Dee, M. Diamantakis, R. Dragani, J. Flemming, R. Forbes, M. Fuentes, A. Geer, L. Haimberger, S. Healy, R. J. Hogan, E. Hólm, M. Janisková, S. Keeley, P. Laloyaux, P. Lopez, C. Lupu, G. Radnoti, P. de Rosnay, I. Rozum, F. Vamborg, S. Villaume, J.-N. Thépaut, The ERA5 global reanalysis. *Q. J. Roy. Meteorol. Soc.* **146**, 1999–2049 (2020).

Acknowledgments: We acknowledge the CMIP5 and COWCLIP projects for making data available. We also acknowledge A. Bugnot for providing the global dataset of offshore and coastal infrastructure and P. Camus and C. Izaguirre for providing the global database of open-coast ports. We also thank T. Shimura for providing the Japanese wave buoy dataset. **Funding:** J.M. acknowledges support of the University of Central Florida (UCF) Pre-eminent Postdoctoral Program (P3) and the NASA Sea Level Change Team, SLCT. T.W. acknowledges support of the National Science Foundation (NSF) (through grant number 2141461). S.V. acknowledges support by the U.S. Geological Survey (USGS). I.Y. acknowledges the financial support of the Australian Research Council (grant number DP210100840). M.H. is supported by the Australian Commonwealth National Environmental Science Program (NESP) and CSIRO's Climate Science

Centre. **Author contributions:** J.M. conceived the analysis. J.M. and T.W. conducted the technical analysis with contributions from S.V. and S.S.-A. J.M. wrote the manuscript with input from all coauthors, including I.Y. and M.H. **Competing interests:** The authors declare that they have no competing interests. **Data and materials availability:** The raw climate datasets used in the analysis are available within the CSIRO data servers (COWCLIP datasets) at https://thredds.aodn.org.au/thredds/catalog/CSIRO/Climatology/COWCLIP2/catalog.html. The wave buoy data are available from the European Union's (EU) Earth observation Programme Copernicus online database (see www.copernicus.eu/en/access-data), the National Data Buoy Center (NDBC) (see www.ndbc.noaa.gov/obs.shtml), and the Australian Integrated Marine Observing System (IMOS): https://imos.org.au/facilities/nationalmooringnetwork/wave-buoys. All data needed to evaluate the conclusions in the paper are present in the paper and/or the Supplementary Materials.

Submitted 8 August 2022
Accepted 9 December 2022
Published 11 January 2023
10.1126/sciadv.ade3170

ScienceAdvances

Understanding uncertainties in contemporary and future extreme wave events for broad-scale impact and adaptation planning

Joao Morim, Thomas Wahl, Sean Vitousek, Sara Santamaria-Aguilar, Ian Young, and Mark Hemer

Sci. Adv. **9** (2), eade3170. DOI: 10.1126/sciadv.ade3170

Science Advances (ISSN 2375-2548) is published by the American Association for the Advancement of Science. 1200 New York Avenue NW, Washington, DC 20005. The title *Science Advances* is a registered trademark of AAAS.